XBAER derived aerosol optical thickness from OLCI/Sentinel-3 observation

Linlu Mei[1], Vladimir Rozanov[1], Marco Vountas[1], John P. Burrows[1], Andreas Richter[1]

[1]Institute of Environmental Physics, University of Bremen, Germany

Abstract

A prolonged pollution haze event occurred in the northeast part of China during December 16 - 21, 2016. To assess the impact of such events, the amounts and distribution of aerosol particles formed in such events need to be quantified. The newly launched Ocean Land Color Instrument (OLCI) onboard Sentinel-3 is the successor of the MEdium Resolution Imaging Spectrometer (MERIS). It provides measurements of the radiance and reflectance at the top of the atmosphere which can be used to retrieve the Aerosol Optical Thickness (AOT) on both synoptic to global scales. In this paper, the recently developed AOT retrieval algorithm - eXtensible Bremen AErosol Retrieval (XBAER) has been applied to data from the OLCI instrument for the first time to inlustrate the feasibility of transferring XBAER to new instrument. The first global retrieval results show similar patterns as MODIS and MISR aerosol products. The AOT retrieved from OLCI is validated by comparison with AERONET observations and a correlation coefficient of 0.819 and bias (root mean square) of 0.115 is obtained. The haze episode is well-captured by the OLCI-derived AOT product. XBAER is shown to retrieve AOT from the observations of MERIS and OLCI.

88

1 Introduction

Haze is an atmospheric phenomenon which is associated with horizontal visibilities of less than l0 km and atmospheric relative humidity (RH) less than 90 % (Liu et al., 2013). Haze occurs as a result of pollution i.e. the release of sulfur dioxide (SO_2), nitrogen oxides (NO_x) and particles or the photochemical production of atmospheric particles (Sezer et al., 2005; Pudasainee et al., 2006). These particles are called aerosol. Aerosol has a variety of effects on climate and environment both directly and indirectly. The direct effect is through scattering which cools the atmosphere and surface system or by absorption of incoming solar radiation which also cools the surface but warms the atmosphere. Indirectly, aerosol impacts on cloud formation and the microphysical properties of clouds, which in turn influence cloud albedo and precipitation (Li et al., 2011) adding to therir negative health impacts. Aerosols are also the carriers of toxic substances such as heavy metals and polycyclic aromatic hydrocarbons (Wilkomirski et al., 2011). In Beijing, under high pollution conditions, the concentrations of sulfate and nitrate have been shown to account for 1/3 of the particle matter (PM_{10}) mass and 2/3 of the $PM_{2.5}$ mass, a part of which is attributed to the additional secondary conversion of SO_4^{2} from SO_2 and NO_3^- from NO_x (Ji et al., 2012). Haze has a significant effect on regional climatic phenomena, such as monsoon (Chung et al., 2002; Evan, et al., 2011) and on the environment e.g. air quality (Lin et al., 2012) and visibility (Zhao et al., 2011). Aerosol can adversely affects human health (Evan, et al., 2011), especially for the elderly, children (American Academy of Pediatrics Committee on Environmental Health, 1993), and even the new-born children (Dadvand et al., 2013).

A thick smoke haze enveloped the Eastern and Northern part of China in December 2016. Pictures taken by cameras onboard the satellite TERRA/AQUA show that the area affected by

111   haze exceeded about 1.5 million square kilometers area of China. The poor visibility resulted in

112   several highways and regional airports being closed for extended periods. The situation

113   deteriorated significantly during the haze event and became a matter of public concern.

114   Satellite observations of the reflectance of solar radiation at the top of the atmosphere are

115   used to determine Aerosol Optical Thickness (AOT), which is used as an indicator of air quality

116   (Kaufman et al., 2002). There are numerous attempts for the retrieval of aerosol properties from

117   satellite observations. AOT retrieval algorithms have been developed for use with the

118   measurements of Moderate Resolution Imaging Spectroradiometer (MODIS) (e.g. Dark-Target

119   (Levy et al., 2013), DeepBlue (Hsu et al., 2013), the Multiangle implementation of atmospheric

120   correction (MAIAC) (Lyapustin et al., 2011)),   Advanced Along-Track Scanning Radiometer

121   (AATSR) (e.g. AATSR Dual-Viewing (ADV) (Kolmonen et al., 2016; Sogacheva et al., 2017),

122   Oxford-RAL Aerosol and Cloud (ORAC) (Thomas et al., 2009) and Swansea University (SU)

123   (North et al., 1999) algorithms). AOT is also derived from observations of the Multi-angle

124   Imaging SpectroRadiometer (MISR) (Diner et al., 2005), PARASOL's Polarization and

125   Directionality of the Earth's Reflectances (POLDER) (Dubovik et al., 2014), Sea-Viewing Wide

126   Field-of-View Sensor (SeaWiFS) (Sayer et al., 2012) etc.

127   One challenge for the derivation of AOT long term datasets from satellite observation is to

128   generate comparable AOT data products from the different instruments, which have limited

129   lifetimes. Consequently mature aerosol algorithms, which can be applied to data from instruments

130   on different platforms, are required. For example, the three MODIS aerosol algorithms have been

131   applied to the Visible Infrared Imaging Radiometer Suite (VIIRS) instrument and the three

132   AATSR algorithms have been proposed to be applied to the observations of the Sea and Land

133   Surface Temperature Radiometer (SLSTR) instrument (Popp et al., 2016).

134   The MERIS instrument onboard Environmental Satellite (Envisat) provided valuable

135   information for different applications (Verstraete et al., 2010). There are several previous attempts

136   to develop AOT retrieval algorithms for MERIS, e.g. the Bremen AErosol Retrieval (BAER; von

137   Hoyningen-Huene et al., 2003, 2011), and the European Space Agency (ESA) standard aerosol

138   retrieval (Santer et al, 2007). These had mixed success (Mei et al., 2017a). BAER has limited

139   accuracy away from dark-vegetated surfaces and primarily for non-absorbing aerosols (de Leeuw

140   et al., 2015; Holzer-Popp et al., 2013) while the ESA standard AOT retrieval tends to overestimate

141   AOT (de Leeuw et al., 2015). The recently developed eXtensible Bremen AErosol (XBAER)

142   algorithm (Mei et al., 2017a , 2017b) has been internally validated in the Aerosol- Climate Change

143   Initiative (Aerosol-CCI) project (Popp et al., 2016), and shows very promising results.

144   The newly launched (on 16th Feb, 2016) instrument Ocean Land Color Instrument (OLCI)

145   takes the heritage of MERIS as it contains all MERIS channels. Theoretically it is possible to

146   transfer the mature MERIS retrieval algorithms to the OLCI instrument. In this paper, the XBAER

147   algorithm has been applied to OLCI instrument for the first time. To our best knowledge, this is

148   the first publication of AOT retrieved from OLCI. Although Sentinel-3 has only recently been

149   launched, applying XBAER to OLCI data we have identified a haze event over Beijing, China

150   during December 2016. We use observations by OLCI during this episode to test our retrieval of

151   AOT.

152   In this manuscript, the characteristics of OLCI and MERIS instruments are presented and

153   compared in Section 2. The XBAER algorithm is briefly explained in Section 3. Section 4 shows

删除的内容: 6

删除的内容: 6

删除的内容: 6

157   the comparison between OLCI and MERIS instruments, first XBAER OLCI-derived AOT results

158   and a comparison with AOT from MODIS/MISR and AERONET observations is shown and

159   discussed from a global point of view. The AOT retrieved during the regional haze event is also

160   presented and discussed in Section 4. The conclusions are given in Section 5.

161
162
163 **2 OLCI instrument**

164   The European Space Agency Sentinel-3 satellite was successfully launched on 16th February 2016.

165   It is one element of the EU Copernicus system previously known as the Global Monitoring for

166   Environment and Security (GMES) system

167   (https://sentinel.esa.int/web/sentinel/user-guides/sentinel-3-olci). The aim of the Sentinel-3

168   mission is to provide data continuity of observation and data products for two of the instruments

169   aboard ENVISAT viz MERIS

170   (https://earth.esa.int/web/guest/missions/esa-operational-eo-missions/envisat/instruments/meris)

171   and AATSR

172   (https://earth.esa.int/web/guest/missions/esa-operational-eo-missions/envisat/instruments/aatsr).

173   There is no overlap of observations because ENVISAT was lost unexpectedly and suddenly in

174   April, 2012. The outstanding performance of ENVISAT over the last decade led both scientists

175   and engineers to believe that it is valuable to make use of multiple sensing instruments to

176   accomplish its operational mission for oceanography & global land applications. The instruments

177   onboard Sentinel-3 include SLSTR (Sea and Land Surface Temperature Radiometer), OLCI

178   (Ocean and Land Colour Instrument), SRAL (SAR Altimeter), DORIS (Doppler Orbitography and

179   Radiopositioning Integrated by Satellite), and MWR (Microwave Radiometer), which can deliver

180   additional information for Sea/Land colour data (at least MERIS quality), Sea/Land surface

181 temperature (at least AATSR quality) , Sea surface topography data (at least Envisat RA quality)

182 (https://earth.esa.int/web/guest/missions/esa-eo-missions/sentinel-3).

183   The primary objective of OLCI is to observe the ocean and land surface in the solar spectral

184 region and thereby to harvest information related to biology. OLCI also provides information on

185 the atmosphere and contributes to climate studies. OLCI is a push-broom imaging spectrometer

186 that measures solar radiation reflected by the Earth, at a ground spatial resolution of 300 meter, in

187 21 spectral bands between 0.4 and 1.02 μm, with a swath width of 1270 km. A comparison

188 between the MERIS and OLCI instruments has been included in Table 1.

189 **Table 1 Spectral channels for MERIS and OLCI instruments**

OLCI			MERIS			Usage
Band #	**Central wavelength**	**Width**	**Band #**	**Central wavelength**	**Width**	**Δ: cloud * Surface ¶:Aerosol**
1	400	15				
2	412.5	10	1	412.5	10	**Δ/*/¶**
3	442.5	10	2	442.5	10	***/¶**
4	490	10	3	490	10	***/¶**
5	510	10	4	510	10	***/¶**
6	560	10	5	560	10	***/¶**
7	620	10	6	620	10	***/¶**
8	665	10	7	665	10	***/¶**
9	673.75	7.5				
10	681.25	7.5	8	681.25	7.5	***/¶**
11	708.75	10	9	708.75	10	***/¶**
12	753.75	7.5	10	753.75	7.5	**Δ**
13	761.25	2.5	11	760.625	3.75	**Δ**
14	764.375	3.75				
15	767.5	2.5				
16	778.75	15	12	778.75	15	
17	865	20	13	865	20	
18	885	10	14	885	10	*****
19	900	10	15	900	10	
20	940	20				
21	1020	40				

190

191

3 XBAER algorithm

The XBAER algorithm was designed for the retrieval of AOT from MERIS and similar observations. It has its own cloud screening approach, aerosol type selection and surface parameterization (Mei et al., 2017a, 2017b). The cloud screening algorithm minimizes cloud contamination for aerosol retrieval in XBAER. The XBAER cloud masking algorithm determines the presence of cloud by using i) the brightness of the scene, ii) the homogeneity or variability of the top of the atmosphere reflectance and iii) cloud height information (Mei et al., 2017b). The threshold values in the XBAER cloud masking algorithm are selected by a two steps process. The ranges for the thresholds were determined by using accurate radiative transfer modeling with different surface and atmospheric scenarios. A histogram analysis has been used for different cloud, aerosol and surface scenarios to estimate the optimal threshold values for each criterion.

The XBAER algorithm uses a generic one-parametric surface parameterization for both land and ocean. XBAER uses a set of space-time dependent spectral coefficients to describe surface properties. The spatial and temporal resolutions are 10 km and monthly, respectively. The surface spectral reflectance can be determined simultaneously with AOT in an iterative procedure (Mei et al., 2017a). This approach assumes that the wavelength-dependent properties of surface spectral reflectance are constrained by space and time dependent spectral coefficients. The wavelength-independent single parameters (Soil-adjusted Vegetation Index (SAVI) for land retrieval and Normalized Differential Pigment Index (NDPI) for ocean retrieval) have been used as the "tuning" parameters. The definitions of SAVI and NDPI are given below.

$$SAVI = \frac{R(\lambda_{14}) - R(\lambda_7)}{R(\lambda_{14}) + R(\lambda_7) + L}(1 + L) . \tag{1}$$

删除的内容: 6

删除的内容: 6

删除的内容: 6

删除的内容: 6

$$L = 1 - \frac{2R(\lambda_{14}) + 1 - \sqrt{(2R(\lambda_{14}) + 1)^2 - 8(R(\lambda_{14}) - R(\lambda_7))}}{2},$$ (2)

where R is the SSR and the subscript for the wavelength denotes the MERIS channel numbers defined in Table 1.

$$NDPI = \frac{R(\lambda_2) - R(\lambda_5)}{R(\lambda_3)}.$$ (3)

In this manner, XBAER is not limited to dark surfaces (ocean, vegetation) and also retrieves AOT over bright surfaces (e.g. desert, semiarid, and urban areas).

XBAER uses MODIS Dark-Target aerosol type assumptions and the expected aerosol type for a given region and season is taken from an analysis of Aerosol Robotic Network (AERONET) and Maritime Aerosol Network (MAN) observations for both land and ocean. AOT and surface reflectance are retrieved by minimizing the difference between simulated and measured TOA reflectance using a Look-Up-Table (LUT), created by the radiative transfer software package SCIATRAN (Rozanov et al., 2014). Details of the XBAER algorithm can be found in Mei et al., (2017a, 2017b). A post-processing technique used in Aerosol-CCI project and the MODIS monthly snow fraction dataset have been additionally applied to avoid unresolved clouds/snow (Popp et al., 2016).

4 Results

4.1 Verification

One important characteristic invetsigated is the instrument spectral response function (SRF) because it is the major difference between MERIS and OLCI for overlap channels. Fig. 1 shows the SRF for the MERIS and OLCI overlap channels. The OLCI RSF mean dataset

244　(https://sentinel.esa.int/web/sentinel/technical-guides/sentinel-3-olci/olci-instrument/spectral-respo

245　nse-function-data) has been used. Differences between MERIS and OLCI SRF are identified but

246　have negligible impact on the retrieved AOT.

247　　In order to quantitatively investigate the impact of different SRFs, the TOA reflectances have

248　been simulated with and without taking SRF into account. The simulations have been determined

249　by undertaking radiative transfer simulations using SCIATRAN for atmospheric and surface

250　conditions (Rozanov et al., 2014).The MERIS observation geometry for the 2nd July 2009 over

251　Paris was used to perform a forward simulation. In particular, the solar zenith angle, viewing angle

252　and relative azimuth were set to (32.32°, 28.7°, 30.65°) as suggested in Mei et al. (2016a).

253　　In order to design representative simulated scenarios, we define a comprehensive set of

254　aerosol optical parameters, surface spectral reflectances, and other atmospheric properties

255　comprising temperature and pressure profiles, the profiles of the concentration of gaseous

256　absorbers and scattering.　Suitable ranges of values for all relevant inputs for the RTM are

257　obtained by statistical analysis of corresponding global products (Mei et al., 2016a). For this

258　purpose, we use:

259　　**Surface reflectance**: Three typical surface types representing vegetation, soil and water, i.e.

260　relatively dark land (vegetation-covered city), bright land (desert), and water surface (ocean

261　surface), were used. The typical vegetation and soil spectra are adapted from von

262　Hoyningen-Huene et al. (2011), the liquid water spectrum comes from the SCIATRAN database

263　(see references in Rozanov et al., 2014). Fig. 2 shows the corresponding surface reflectance

264　spectra for selected surface types.

265　　**Aerosol Scenarios**: Within the ESA Aerosol-CCI project, a representative value for global

266   mean AOT of 0.25 has been selected (Holzer-Popp et al., 2013; de Leeuw et al., 2015). Thus an

267   AOT of 0.25 was selected for the simulation of "vegetation" and "water" cases. An AOT value of

268   0.5 was used for the "soil" scenario to represent a 'real' case for the Sahara region. Moderately

269   absorbing (fine mode radius $r_{v,f}$ = 0.150 μm, coarse mode radius $r_{v,c}$ = 3.19 μm, fine mode variance

270   σ_f = 0.408, coarse mode variance σ_c = 0.754, fine/coarse mode volumes ($\mu m^3/\mu m^3$) are 0.055 and

271   0.038), pure maritime type ($r_{v,f}$ = 0.150 μm, $r_{v,c}$ = 3.19 μm, σ_f = 0.408, σ_c = 0.754, fine/coarse

272   mode volumes ($\mu m^3/\mu m^3$) are 0.04 and 0.296) and dust aerosol model ($r_{v,f}$ = 0.140 μm, $r_{v,c}$ = 1.74

273   μm, σ_f = 0.454, σ_c = 0.687, fine/coarse mode volumes ($\mu m^3/\mu m^3$) are 0.02 and 0.157) were used

274   for aerosol types.

275   **Other atmospheric parameters**: The profiles of temperature, pressure, and concentration of

276   the gases ozone, O_3, nitrogen dioxide, NO_2, and molecular oxygen, O_2 and water vapor, H_2O,

277   which all absorb in the 400 – 900 nm spectral region were provided by the Bremen 2D chemical

278   transport model (Sinnhuber et al., 2009).

279   In Table 1 the spectral channels of OLCI and MERIS are given. Fig. 2 (a) presents the

280   surface spectral reflectance for the three surface types selected. Fig.2 (b) presents the simulated

281   TOA differences for the above scenarios. The differences for all surface/atmospheric conditions

282   are less than 1.5%. These are similar to the simulation with and without convolution for MERIS

283   with the exception of the O2A and water vapor channels. However, the potential impacts of

284   different SRFs may also introduce some uncertainties to the XBAER cloud mask due to relative

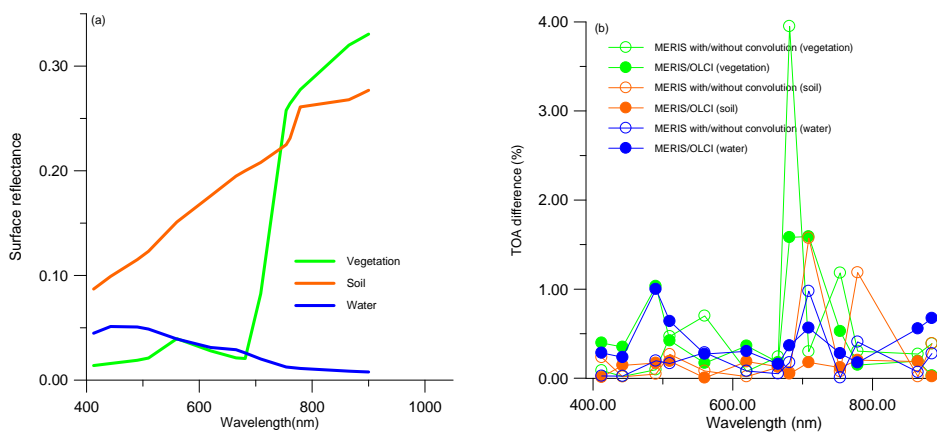285   strong impact of SRF to the O2A channels (about 20% difference).

286

287
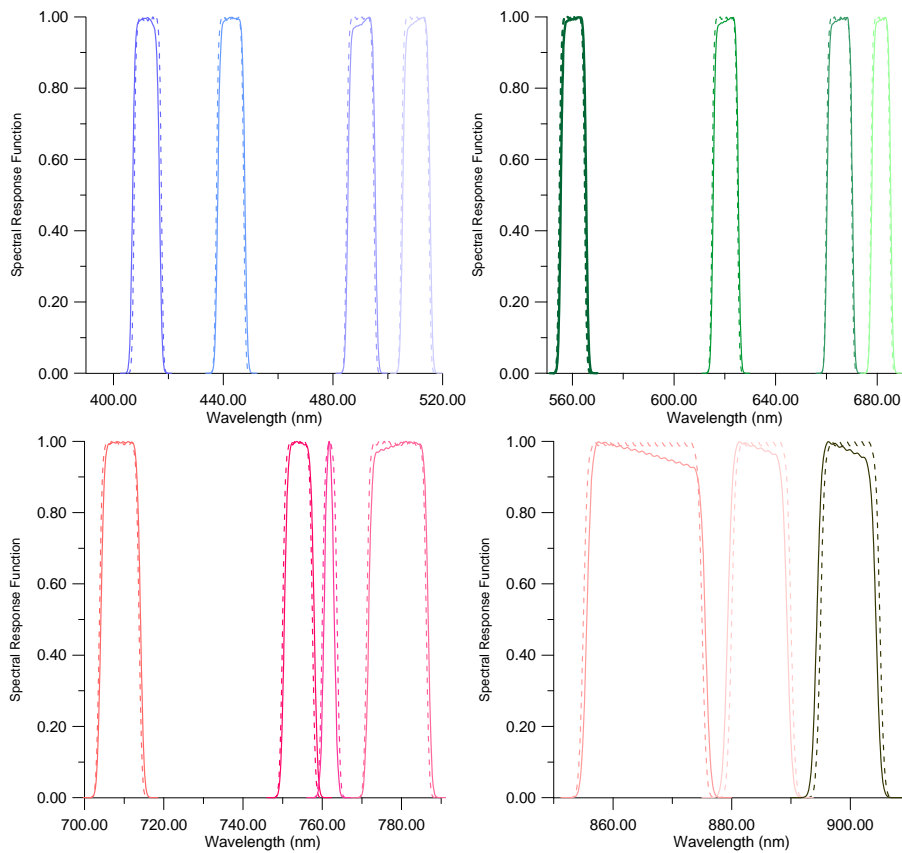
Fig 1 Spectral Response Function of MERIS (dash lines) and OLCI (solid lines) for overlap

channels

290

291

Fig 2 (a) Surface reflectances of the three selected surface types; (b) Comparisons of the simulated

TOA reflectance for different combinations of MERIS and OLCI SRF values. Green, yellow and

blue colors in (a) and (b) represent vegetation, soil and water simulations. Filled circles in (b) are

differences for simulations using MERIS and OLCI SRFs. Circles in (b) are differences for

simulations with and without convolution.

4.2 First XBAER AOT retrieval for OLCI and its validation

299

300 AERONET observations are considered to be the "ground truth" for satellite validation (Holben et

301 al., 1998). Here, we collocate the XBAER OLCI aerosol retrievals with the AERONET Version

302 3.0 (https://aeronet.gsfc.nasa.gov/new_web/Documents/AERONET-V3_News_Final.pdf. last

303 access: 15 May, 2017), Level 1.5 (Level 2.0 for both AERONET Version 2.0 and 3.0 are not

304 available till 15 May, 2017) (Holben et al., 1998; Smirnov et al., 2000). As AERONET does not

305 provide AOT at 0.55 μm, data are interpolated to 0.55 μm using quadratic fits on a log-log scale

306 (Eck et al., 1999). Since AERONET provides a point measurement with high-temporal resolution

307 while satellite observations represent a 'regional' measurement depending on the satellite spatial

308 resolution for a particular overpass time, spatial statistics for the OLCI data are calculated and

309 compared to the temporal statistics of the AERONET observations taken within ±30 min of OLCI

310 overpass following the spatial-temporal technique of Ichoku et al. (2002).

311 Fig. 3 is a plot which compares XBAER-derived and AERONET observed AOT at 0.55 μm.

312 The collocations of Fig.3 contain various surface and aerosol types, which ensure a wide

313 representativeness of the validation. 733 collocations were found for December 2016. The colour

314 of each ordered pair (0.025 × 0.025 increment) represents the number of such matchups. Negative

315 AOT (> -0.1) values are possible and reasonable as a result of the noise in satellite observations

316 (Levy et al., 2007) and uncertainties of surface parameterization. The comparison here excluded

317 negative values and only AOT values between 0.0 and 2.5 are used following the validation

318 method of other aerosol products (Sayer et al., 2012; Levy et al., 2013). The validation contains

319 various surface and aerosol types, which ensures a wide representativeness of the validation. The

320 regression equation is y = (0.81x ± 0.04) + (0.11 ± 0.01) with slightly higher correlation compared

321 to the first MERIS validation (*R*=0.82 vs R=0.78) (Mei et al., 2016a). The AOT is

322 reasonable-correlated between the two datasets (R = 0.82), with increased scatter for high aerosol

323 loadings. The majority of the data (87.5%) are for low aerosol loadings (AOT<0.3). The

324 comparison between XBAER AOTs and AERONET observations shows the acceptable quality of

325 the first OLCI XBAER results.

326   Fig. 4 shows the global monthly AOT of December 2016 for MODIS collection 6 (Levy et al.,

327 2013), MISR (Diner et al., 2005) and OLCI (XBAER) algorithm. In order to identify biomass

328 burning   events,   the   active   fire   points   of   MODIS

329 (https://lance.modaps.eosdis.nasa.gov/cgi-bin/imagery/firemaps.cgi) are added to the figures.

330 Please note that the MISR "FIRSTLOOK" product is used because the monthly Land Surface and

331 Aerosol products are not yet processed for December 2016 (Personal communication with NASA

332 Langley ASDC on 16 February 2017). MODIS/MISR on board of TERRA and OLCI on board of

333 Sentinel-3 have very similar overpass time (within 30 minutes difference). Therefore, all four

334 results should show similar patterns for large AOT from desert dust events over Sahara, biomass

335 burning over West Africa and Amazon region and anthropogenic pollution over India and East

336 Asia. In Fig.4, XBAER AOT from OLCI shows similar patterns as the AOT from MODIS and

337 MISR for both land and ocean. However, there are differences in the magnitude of the AOTs.

338 Biomass burning over Africa, as observed in the MODIS active fire product, produces a 'plume

339 belt' of high AOT near the equator. This is observed in all three AOT products. The AOT

340 distribution pattern over India, which depends on the unique meteorological conditions and

341 emissions is captured by the three AOT data products as well. MODIS and OLCI show similar

342 pattern and magnitude of large AOT over Eastern China while the values from MISR are slightly

13

343 lower, which may be due to the relative small sampling compared to MODIS and OLCI. However,

344 the retrievals from XBAER over Australia are higher than those of MODIS and MISR. In addition

345 to potential contamination by thin clouds observed in the RGB composite figures, the calibration

346 uncertainties associated with a new instrument may also contribute to the bias of XBAER derived

347 AOT. The large AOT differences over Sahara may go, in part, back to different assumptions in the

348 different algorithms for bright surfaces (Lyapustin et al., 2011b; Mei et al., 2016a). Different

349 patterns over Amazon can most likely be attributed to the use of different cloud screening methods.

350 The global patterns obtained indicate that the generic XBAER algorithm works over both dark and

351 bright surfaces using its flexible surface parameterization approach. For relative dark surfaces, the

352 one-parametric surface parameterization is dominated by the first term (SAVI or NDPI tuned term)

353 making XBAER behave like the Dark-Target-like retrieval algorithm. For bright surfaces such as

354 desert, XBAER becomes similar to the DeepBlue AOT retrieval algorithm.
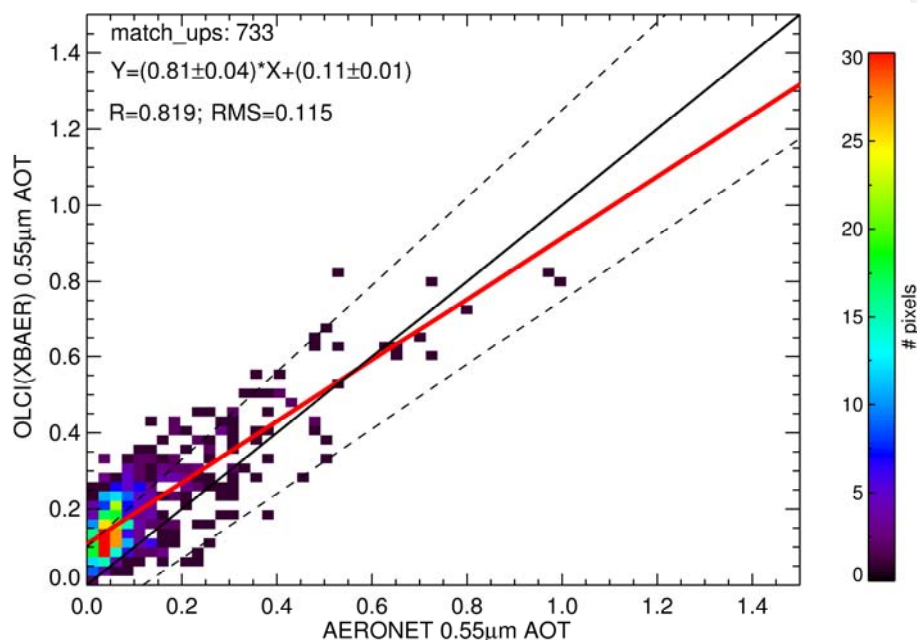
355

356

357 Fig.3 Global comparison of OLCI XBAER AOT with AERONET observations for 2016

358 December. R and 'match_ups' refer to the Pearson correlation coefficient and the number of

359 locations used in the validation respectively. The dashed lines are $\pm 15\%\tau\pm 0.10$
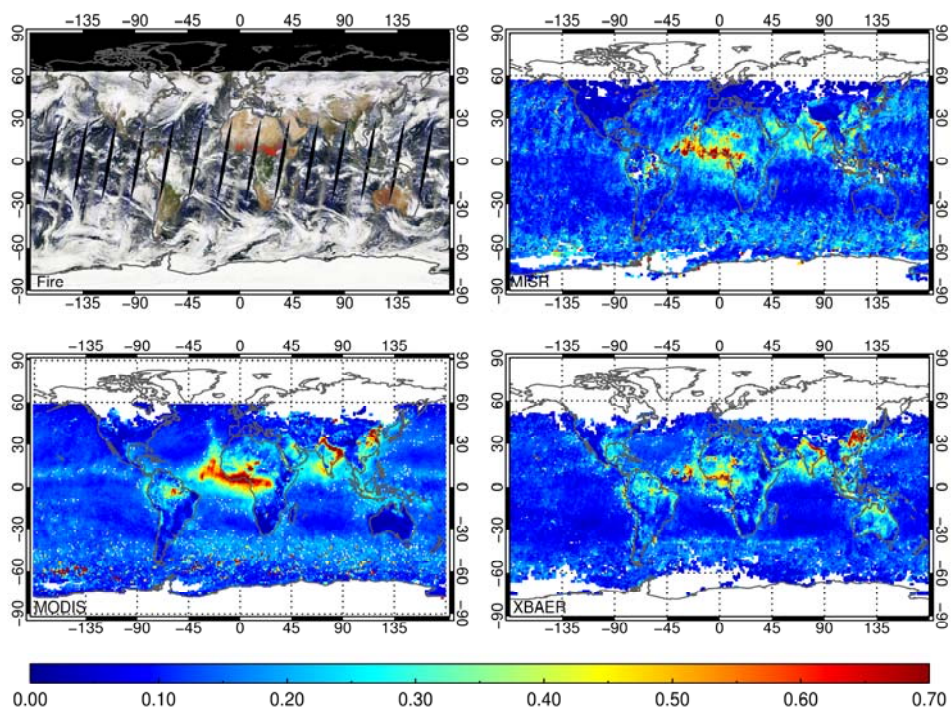
360

362 Fig. 4 Comparison of the retrieved global monthly mean AOT at 0.55 μm for December 2016.

363 Upper row: left – MODIS fire product, right-MISR. Lower row: left-MODIS (Dark-Target and

364 DeepBlue combined), right- OLCI (XBAER)

365

366 **4.3 Beijing Haze event observed by OLCI**

367 In the following we show the ability of the retrievals of XBAER used with OLCI data to resolve

368 spatial aerosol patterns on a synoptic scale. A prolonged haze event was observed over Beijing

369 during the period of 16 – 21 December 2016. The intention of applying XBAER to this event is to

370 show the potential of the retrieval to resolve aerosol patterns at a local level and thus being able to

15

371   support future studies analyzing such events. This event is investigated by both ground-based

372   measurements and satellite observations. Fig.5 (a) shows that winds at the surface were weak with

373   a daily averaged wind speed lower than 3.5 m/s during the period, causing the accumulation of

374   pollutants on a regional scale. The low temperature and high surface pressure near the surface

375   indicate relatively stable atmospheric conditions in the vertical direction (Fig. 5 (b) (c)). The

376   dispersion of pollutants out of the boundary layer is therefore slow. The relative humidity

377   remained high (Fig. 5 (b)) causing the aerosol particles size to increase by the uptake of water

378   (*Winkler*, 1988), thus making the haze event stronger. Under these meteorological conditions,

379   pollutants can accumulate over the North China Plain (NCP) (*Li et al.*, 2011).

380   Fig. 5 (d) shows the time series of concentration of SO_2 and NO_2 in the boundary layer

381   provided by ground-based measurements. The concentrations of SO_2 and NO_2 for haze periods are

382   three to five times larger than those on relatively clear days. We thus assume anthropogenic

383   activities to be the major source of AOT. Fig. 5 (e) and (f) show the AOT from AERONET sites

384   and the time series of the daily mean concentration of $PM_{2.5}$ in Beijing with clearly increased

385   values in the same timespan (16 – 21 December). The lack of larger AOT values observed by

386   AERONET is likely going back to too strict cloud screening procedures. The daily mean

387   concentrations of $PM_{2.5}$ during 16 – 21 December 2016 ranged from 107.1 $\mu g/m^3$ to 394.5 $\mu g/m^3$,

388   which is far above the daily $PM_{2.5}$ limit of the new threshold value set as the Chinese Ambient Air

389   Quality   standard   (75 $\mu g/m^3$)

390   (http://transportpolicy.net/index.php?title=China:_Air_Quality_Standards).   A   large   Angstrom

391   coefficient (Fig. 5(e)) shows that fine particles dominate during this period. In summary, we find

392   that the cause of the haze event in Beijing and northeastern China goes back to: (1) The stable
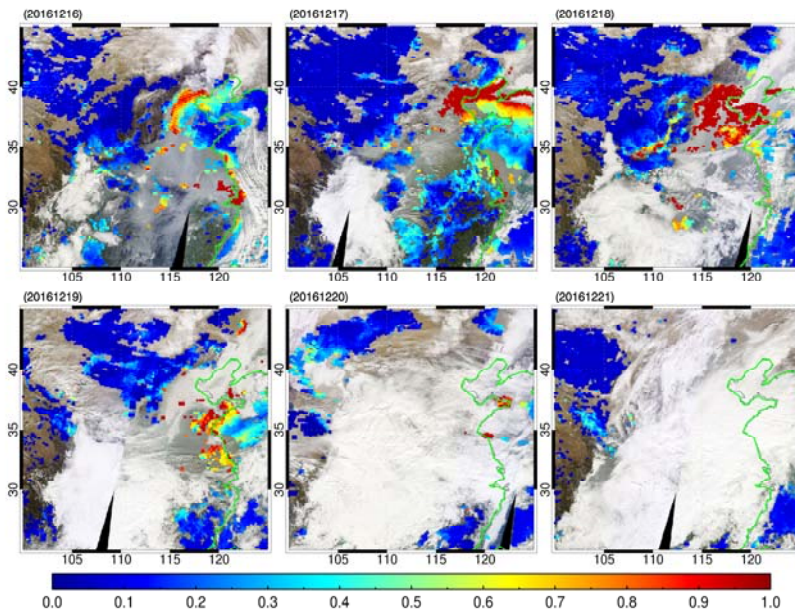
16

393   meteorological conditions (low wind sppeds and temperature inversion) (2) Local emissions (3)

394   High relative humidity.

395   Fig 6 shows the MODIS/Terra derived AOT for the haze period. According to Fig. 6, this

396   intense part of the haze episode has been partly observed by MODIS. However, a large part of it

397   (under cloud free conditions) during the first three days is missing, mainly due to cloud masking

398   applied in the MODIS aerosol retrieval. Fig. 7 shows the AOT from Modern-Era Retrospective

399   analysis for Research and Applications, Version 2 (MERRA-2) simulation (Rienecker et al., 2011)

400   in order to exclude the impact from cloud screening. According to Fig. 7, the shape of the area

401   covered by high AOT in MERRA remains stable except for 20 December, indicating the relative

402   stable meteorological condition during the haze period. Due to the narrower swath width of OLCI

403   compared to that of MODIS (1270 km vs 2300 km), OLCI has a longer 'revisit' time for a

404   repetitive observation of the ground scene in Beijing. According to Fig. 6 and Fig. 8, XBAER

405   discards fewer clear sky ground scenes than the MODIS retrieval, in particular on the 18th and

406   19th of December over Eastern China. For this period, the aerosol over Eastern China has been

407   characterized as 'moderately absorbing aerosol'. The SSA at 0.675 μm from AERONET has

408   values between 0.88 and 0.91, indicating relatively strong absorption from anthropogenic

409   activities. The magnitude of AOT for the overlap regions between OLCI and MERRIA are

410   comparable according to Fig. 7 and Fig. 8. The regions of high aerosol agree well with the aeras

411   having high NO_2 columns in Global Ozone Monitoring Experiment 2 (GOME2) (Richter et al.,

412   2011) for the corresponding time period as presented in Fig. 9. Fig. 8 illustrates that cloud

413   masking, surface treatment and aerosol type selection in XBAER all work well for the detection of

414   extreme haze events. Studies like the one by Zheng et al. (2015), are usually focusing on the origin

415 of such plumes and the speciation of aerosol particles on a city level. XBAER results utilizing

416 multi-spectral imagery such as provided by OLCI can support this kind of studies to identify

417 plume transport and extension. This implies that the OLCI instrument can provide important data

418 on AOT for atmospheric research.
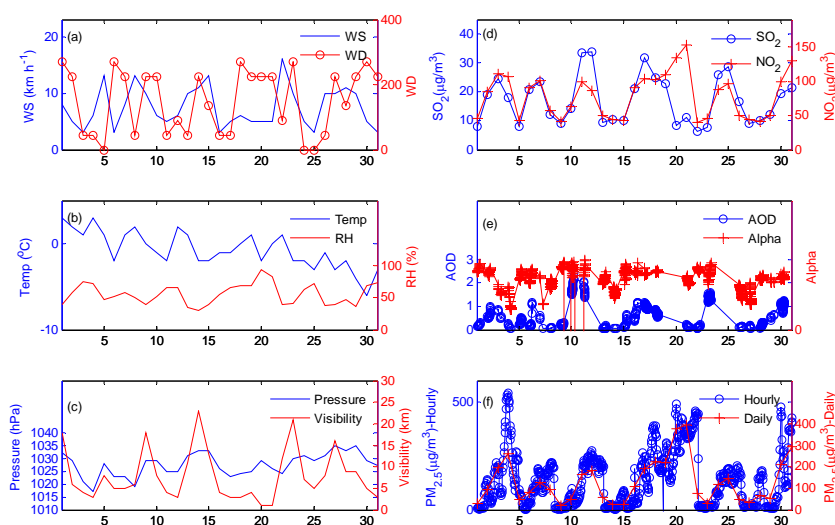
419

420 Fig. 5 Time series of meteorological parameters and pollutants during December 2016. (a)wind

421 direction and wind speed (km/h), (b) temperature (˚ C) and relative humidity (%) , (c) atmospheric

422 pressure (hPa) and visibility (m), (d) SO_2 and NO_2 concentration ($\mu g/m^3$) (e) AOT and Angstrom

423 coefficient (440-870nm) (Alpha)(f) $PM_{2.5}$ hourly and daily concentration($\mu g/m^3$). The atmospheric

424 components and meteorological data are from https://www.aqistudy.cn/historydata/index.php and

425 https://www.wunderground.com/

427   Fig. 6 Daily MODIS RGB and AOT for East China [100º - 125 º E, 25 º- 45 º N] during 16 – 21

428   December 2016 (from top left to bottom right)
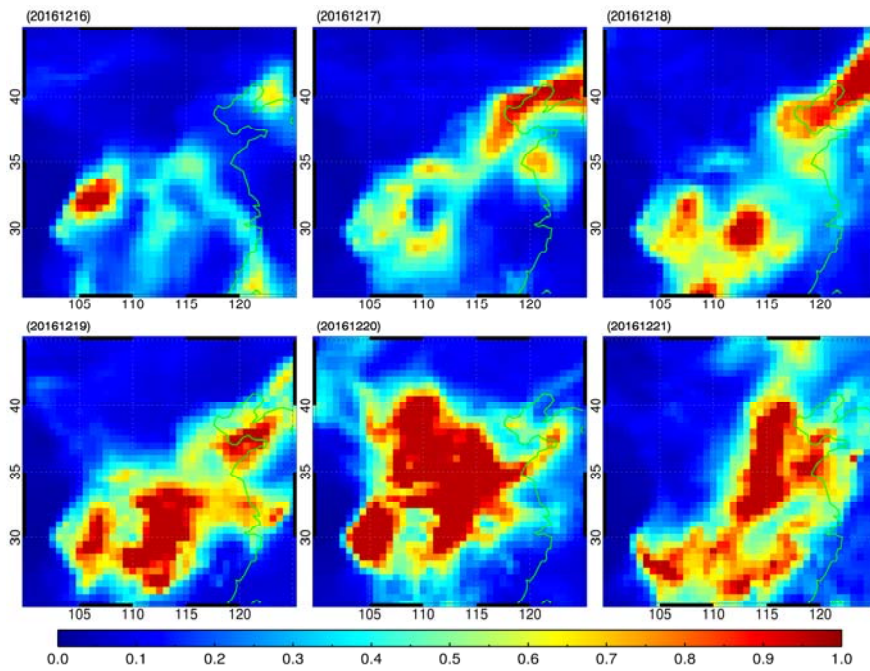
429
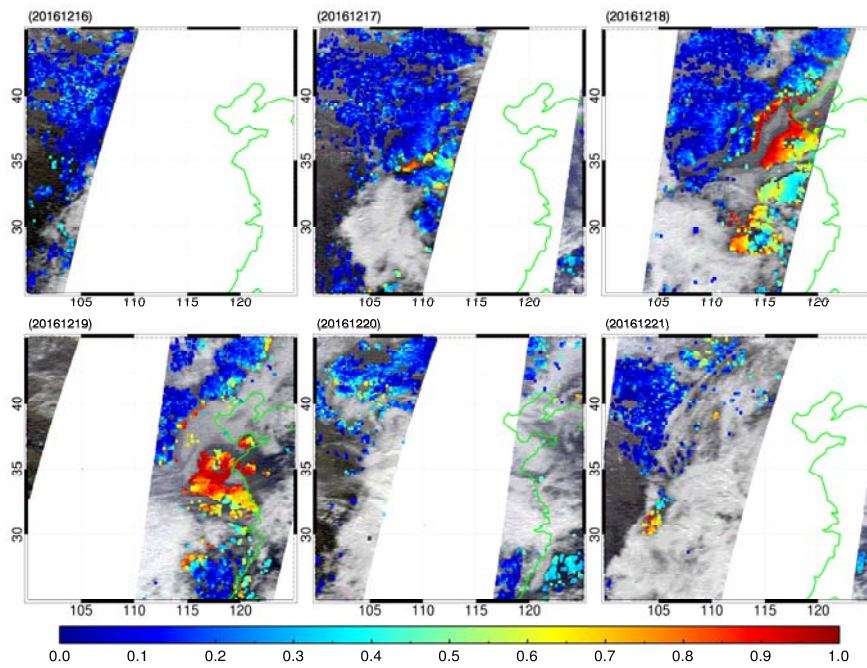430   Fig. 7 Same as Fig. 6 but for MERRA AOT
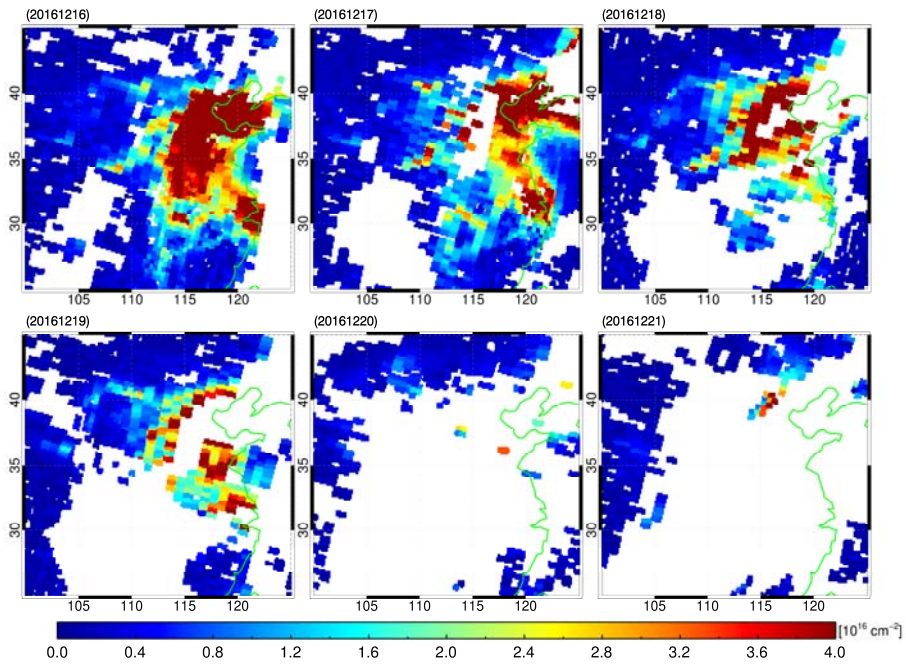
431

432

Fig. 8 Same as Fig. 6 but for OLCI

Fig. 9 Same as Fig. 6 but for NO$_2$ from GOME2a/GOME2b combined IUP-UB product

5 Discussions

In this study, we have applied XBAER to data from the OLCI instrument onboard Sentinel-3 for the first time on both synoptic and global scale. The potential differences caused by different spectral response functions for OLCI and MERIS have been investigated by using SCIATRAN to generate representative simulated scenarios for dust aerosol type over desert, moderately absorbing aerosol over vegetation regions and maritime aerosol over water. The overall differences for all selected channels for XBAER are smaller than 1.5%. This implies that XBAER can be used to retrieve AOT from OLCI. Although relatively large differences caused by SRFs (approximately 20%) have been found for the O_2A channels, the global retrieval of OLCI shows that the original MERIS cloud masking, which includes the use of O_2A channels, works well for OLCI and can potentially even be improved as only MERIS-heritage channels have been used so far with OLCI.

The global monthly mean XBAER AOT maps for December 2016 show good agreement with those by MODIS and MISR. The comparison with AERONET measurements reveals that XBAER can provide promising results over both dark and bright surface. The first comparison with AERONET shows acceptable agreement between the two data sets, with a regression yielding $y = (0.81x \pm 0.04) + (0.11 \pm 0.01)$ and correlation of R=0.82. The global retrievals confirm that XBAER is valid for both dark and bright surfaces because of its use of an optimized monthly global SSR spectral coefficients dataset.

A significant haze event during December 2016 over Beijing has been analyzed in this paper based on ground-based and satellite observations to show the potential of the retrieval to resolve aerosol patterns at a local level and thus being able to support future studies analyzing such events. This large haze event has been attributed to the large local emissions under unfavorable

464   meteorological conditions (temperature inversion in vertical direction and no advection). The

465   MODIS/Terra and OLCI derived AOT both detect the haze event. However, due to cloud

466   screening, the MODIS AOT partly misses it while OLCI AOT is able to detect the main pattern of

467   haze for clear conditions. The overlap retrieval for both MODIS and OLCI has similar values,

468   indicating that OLCI provides another useful data source for air pollution monitoring.

469   Although the study shows that XBAER can be applied to OLCI observations for synoptic to

470   global applications, several important issues need to be addressed in the future work. Potential

471   cloud contamination due to both the relative large calibration uncertainty of OLCI compared to

472   MERIS as well as the impact of SRF on O_2A channel need to be investigated with the new version

473   of level 1 TOA reflectance dataset. Modification or improvement for OLCI cloud screening will

474   be included besides the criteria of brightness, texturing/variability and cloud altitude of the scenes

475   (Mei et al., 2016b). The underestimation of AOT over regions like Sahara could be explained by

476   the spheroid dust model adapted from MODIS-DT algorithm due to the impact of non-sphericity

477   of dust particles on the aerosol phase function (Mei et al., 2016a), a new spheroid model

478   accounting for aerosol particle non-sphericity will be included in the new version (Dubovik et al.,

479   2006). The cloud screening evaluation shows that approximately $5 - 10$ % clouds may be

480   misclassified as retrievable clear cases for MERIS (Mei et al., 2016b) which introduces both bias

481   and potential patchiness of XBAER derived AOT for OLCI. Thus a new cloud post-processing,

482   following the AATSR dual-view (ADV) algorithm (Sogacheva et al., 2017), will be applied to

483   discard the pixels that might potentially be affected by cloud (cloud edge, very thin cloud and so

484   on).

485

Reference

American Academy of Pediatrics Committee on Environmental Health (1993), Ambient Air Pollution: Respiratory Hazards to Children., *Pediatrics*, 91 (6), 1993,1210-1213.

511   Chen, Z.H., Cheng, S.Y., Li, J.B., Guo, X.R., Wang, W.H., Chen, D.S.(2008), Relationship

512   between atmospheric pollution processes and synoptic pressure patterns in northern China. *Atmos.*

513   *Environ.*, 42 (24), 6078 – 6087, doi : http://dx.doi.org/10.1016/j.atmosenv.2008.03.043.

514

515   Chung, C. E., Ramanathan, V. And Kiehl, J.T.(2002), Effect of the South Asian Absorbing Haze

516   on the Northeast Monsoon and Surface-Air Heat Exchange,   *J. Climate*, 15, 2462-2476, doi :

517   http://dx.doi.org/10.1175/1520-0442(2002)015<2462:EOTSAA>2.0.CO;2

518

519   Dadvand, P., Parker, J., Bell, M. L., Bonzini, M., Brauer, M., Darrow, L.A., Gehring, U.,

520   Glinianaia, S.V., Gouveia, N., Ha, E –h, Leem, J. H., van den Hooven, E. H., Jalaludin, B., Jesdale,

521   B. M., Lepeule, J., Morello-Frosch, R., Morgan, G.G., Pesatori, A.C., Pierik,F.H., Pless-Mulloli,

522   T., Rich,D. Q., Sathyanarayana, S., Seo, J., Slama, R., Strickland, M., Tamburic, L., Wartenberg,

523   D., Nieuwenhuijsen, M.J., Woodruff, T.J. (2013), Maternal exposure to particulate air pollution

524   and term birth weight : a multi-country evaluation of effect and heterogeneity., *Environ. Health*

525   *Perspect.*, 121, 367-373, doi :http://dx.doi.org/10.1289/ehp.1205575.

526

527   deLeeuw, G., Holzer-Popp, T., Bevan, S., Davies, W., Descloitres, J., Grainger, R., Griesfeller, J.,

528   Heckel, A., Kinne, S., Klüser, L., Kolmonen, P., Litvinov, P., Martynenko, D., North, P., Ovigneu

529   r,B., Pascal, N., Poulsen, C., Ramon, D., Schulz, M., et. al. (2015). Evaluation of seven European

530   aerosol optical depth retrieval algorithms for climate analysis. *Remote Sensing of Environment*,

531   162, 295-315.

532

533 Dubovik, O., Lapyonok, T., Litvinov, P., Herman, M., Fuertes, D., Ducos, F., Torres, B., Derimian,

534 Y., Huang, X., Lopain, A., Chaikovsky, A., Aspetsberger, M., Federspiel, C., (2014), GRASP: a

535 versatile algorithm for characterizing the atmosphere, *SPIE Newsroom*. 1-4, DOI:

536 10.1117/2.1201408.005558

537

538 Diner, D. J., Martonchik, J. V., Kahn, R. A., Pinty, B., Gobron, N., Nelson, B. N., and Holben, B.

539 N. (2005), Using angular and spectral shape similarity constraints to improve MISR aerosol and

540 surface retrievals over land, *Remote Sens. Environ.*, 94, 155–171.

541

542 Dubovik, O., Sinyuk, A., Lapyonok, T., Holben, B.N., Mishchenko, M., Yang, P., Eck. T.F.,

543 Volten, H., Munoz, O., Veihelmann, B., van der Zande, W. J., Leon, J.-F., Sorokin, M., and

544 Slutsker, I. (2006), Application of spheroid models to account for aerosol particle nonsphericity in

545 the remote sensing of desert dust, *Journal of Geophysical Reserch*, 111 (D11208),

546 doi :10.1029/2005JD006619.

547

548 Eck, T. F., Holben, B. N., Reid, J. S., Dubovik, O., Smirnov, A., O'Neill, N. T., et al.: Wavelength

549 dependence of the optical depth of biomass burning, urban, and desert dust aerosols, *Journal of*

550 *Geophysical Research: Atmospheres*, 104(D24), 31333–31349, 1999

551

552 Evan, A.T., Kossin, J.P., Chung, C.E and Ramanathan, V.(2011), Arabian Sea tropical cyclones

553 intensified by emissions of black carbon and other aerosols, *Nature*, 479, 94-97,

554 doi:10.1038/nature10552.

555

Holzer-Popp, T. Leeuw, G. Griesfeller, J. Martynenko, D. Klüser, L. Bevan, S. Davies, W. Ducos, F.Deuzé, J. Graigner, R. Heckel, A. Hoyningen-Hüne, W. Kolmonen, P. Litvinov, P. North, P.Poulsen, C. Ramon, D. Siddans, R. Sogacheva, L. Tanre, D. Thomas, G. Vountas, M. Descloitres,J. Griesfeller, J. Kinne, S. Schulz, M. & Pinnock, S. (2013). Aerosol retrieval experiments in the ESA Aerosol_cci project. *Atmospheric Measurement Techniques* ,6(8), 1919-1957.

Hsu, N. C., Jeong, M.-J., Bettenhausen, C., Sayer, A. M., Hansell, R., Seftor, C. S., Huang, J., Tsay, S.-C. (2013), Enhanced Deep Blue aerosol retrieval algorithm: The second generation. *Journal of Geophysical Research: Atmospheres*, 118, 9296–9315, doi:10.1002/jgrd.50712, 2013.

Holben, B. N., Eck, T. F., Slutsker, I., Tanre, D., Buis, J. P., Setzer, A., Vermote, E., Reagan, J.A., Kaufman, Y. J., Nakajima, T., Lavenu, F., Jankowiak, I., & Smirnov, A. (1998). AERONET – A federated instrument network and data archive for aerosol characterization. *Remote Sensing of Environment*, 66, 1–16.

Ichoku, C., Chu, D., Mattoo, S., Kaufman, Y. J., Remer, L., Tanre, D., et al.: A spatio-temporal approach for global validation and analysis of MODIS aerosol products, *Geophys. Res. Lett.*, 29(12), 1616, doi:10.1029/2001GL013206, 2002.

Ji, D.S., Wang, Y.S., Wang, L.L., Chen, L.F., Hu, B., Tang, G. Q., Xin, J. Y., Song, T., Wen, T.X., Sun, Y., Pan, Y. P. And Liu, Z. R.(2012), Analysisi of heavy pollution episodes in selected cities

577 of   northern   China,   *Atmos.   Res.*,   50,   338-348,   doi :

578 http://dx.doi.org/10.1016/j.atmosenv.2011.11.053.

579

580 Kaufman, Y.J., Tanre, D., Boucher, O. (2002), A satelite view of aerosols in the climate system,

581 *Nature*, 419, 215-223 (12 September 2002) | doi:10.1038/nature01091

582

583 Kolmonen, P., Sogacheva, L., Virtanen, T. H., de Leeuw G., Kulmala, M. (2016), The

584 ADV/ASV AATSR aerosol retrieval algorithm: current status and presentation of a full-mission

585 AOD   dataset,   *International   Journal   of   Digital   Earth*,   9(6),   545-561,   DOI:

586 10.1080/17538947.2015.1111450

587

588 Levy, R. C., Mattoo, S., Munchak, L. A., Remer, L. A., Sayer, A. M., Patadia, F., Hsu, N. C.

589 (2013), The Collection 6 MODIS aerosol products over land and ocean. *Atmospheric*

590 *Measurement Techniques*, 6, 2989-3034.

591

592 Li, Z.Q., Li, C., Chen, H., Tsay, S. –C., Holben, B., Huang, J., Li, B., Maring, H., Qian, Y., Shi,

593 G., Xia, X., Yin, Y., Zheng,Y. And Zhuang, G.(2011), East Asian Studies of Tropospheric

594 Aerosols and their Impact on Regional Climate (EAST-AIRC): An overview, *J. Geophys. Res.*,

595 116, D00K34, doi:10.1029/2010JD015257.

596

597 Lin, M., Tao, J., Chan, C.Y., Cao, J. J, Zhang, Z. S., Zhu, L.H. and Zhang, R.J.(2012), Regression

598 analyses between recent air quality and visibility changes in megacities at four haze regions in

599 China, *Aerosol and Air Quality Research*, 12, 1049 – 1061, doi: 10.4209/aaqr.2011.11.0220.

600

601 Liu, X. G., Li, J., Qu, Y., Han, T., Hou, L., Gu, J., Chen, C., Yang, Y., Liu, X., Yang, T., Zhang, Y.,

602 Tian, H., and Hu, M.: Formation and evolution mechanism of regional haze: a case study in the

603 megacity Beijing, China, *Atmos. Chem. Phys.*, 13, 4501-4514, doi:10.5194/acp-13-4501-2013,

604 2013.

605

606 Lyapustin, A., Wang, Y., Laszlo, I., Kahn, R., Korkin, S., Remer, L., Levy, R., Reid, J. S. (2011),

607 Multiangle implementation of atmospheric correction (MAIAC): 2. Aerosol algorithm. *Journal of*

608 *Geophysical Research-Atmospheres*, 116, D03211, doi: 10.1029/2010JD014986.

609

610 Mei, L., Rozanov, V. V., Vountas, M., Burrows, J. P., Levy, R. C., & Lotz, W.A. (2017a). Retrieval

611 of aerosol optical properties using MERIS observations: algorithm and some first results. *Remote*

612 *sensing of Environment*,197,125 – 141, http://dx.doi.org/10.1016/j.rse.2016.11.015

613

614 Mei, L. L., Vountas, M., Gómez-Chova, L., Rozanov, V., Jäger, M., Lotz, W., Burrows, J.P., &

615 Hollmann, R. (2017b). A Cloud masking algorithm for the XBAER aerosol retrieval using MERIS

616 data, *Remote Sensing of Environment*, 197, 141 – 160, http://dx.doi.org/10.1016/j.rse.2016.11.016

617

删除的内容: 6

删除的内容: .

删除的内容: 6

删除的内容: .

622   North, P., Briggs, S., Plummer, S. & Settle, J. (1999). Retrieval of land surface bidirectional

623   reflectance and aerosol opacity from ATSR-2 multiangle imagery. *IEEE Transactions on*

624   *Geoscience and Remote Sensing* ,37(1), 526-537.

625

626   Pudasainee, D., Sapkota, B., Shrestha, M.L., Kaga, A., Kondo, A., Inoue, Y. (2006), Ground level

627   ozone concentrations and its association with NOx and meteorological parameters in Kathmandu

628   valley,   Nepal,   *Atmos.   Environ.*,   40,   8081–8087,   doi :

629   http://dx.doi.org/10.1016/j.atmosenv.2006.07.011.

630

631   Popp, T., deLeeuw, G., Bingen, C., Brühl, C., Capelle, V., Chedin, A., Clarisse, L., Dubovik, O.,G

632   rainger, R., Griesfeller, J., Heckel, A., Kinne, S., Klüser, L., Kosmale, M., Kolmonen, P., Lelli,L.,

633   Litvinov, P., Mei, L., North, P., et. al. (2016). Development, Production and Evaluation of Aerosol

634   Climate Data Records from European Satellite Observations (Aerosol_cci). *Remote Sensing*, 8(5),

635   421

636

637   Richter, A., Begoin, M., Hilboll, A. & Burrows, J. P.: An improved NO2 retrieval for the

638   GOME-2   satellite   instrument,   *Atmos.   Meas.   Tech.*,   4(6),   1147–1159,

639   doi:10.5194/amt-4-1147-2011, 2011.

640

641   Rienecker, M. M., Suarez, M. J., Gelaro, R., Todling, R., Bacmeister, J., Liu, R., Bosilovich, M.

642   G., Schubert, S. D., Takacs, L., Kim, G-K, Bloom, S., Chen, J., Collins, D., Conaty, A., da Silva,

643   A., Gu, W., Joiner, J., Koster, R. D., Lucchesi, R., Molod, A., Owens, T., Pawson, S., Pegion, P.,

644 Redder, C. R., Reichle, R., Robertson, F. R., Ruddick, A. G., Sienkiewicz, M., and Woollen,

645 J.(2011), MERRA: NASA's Modern-Era Retrospective Analysis for Research and Applications, J.

646 Climate, 24, 3624–3648.

647

648 Rozanov, V., Rozanov, A., Kokhanovsky, A., & Burrows, J. (2014). Radiative transfer through

649 terrestrial atmosphere and ocean: software package SCIATRAN. *Journal of Quantitative*

650 *Spectroscopy & Radiative*, 133, 13–71.

651

652 Santer, R., Ramon, D., Vidot, J., & Dilligeard, E. (2007). A surface reflectance model for aerosol

653 remote sensing over land. *International Journal of Remote Sensing*, 28, 737–760.

654

655 Sayer, A. M., Hsu, N. C., Bettenhausen, C., Ahmad, Z., Holben, B., Smirnov, A., Thomas, G. E.,

656 and Zhang J. (2012), SeaWiFS Ocean Aerosol Retrieval (SOAR): Algorithm, validation, and

657 comparison with other data sets, *Journal of Geophysical Research*, 117, D03206,

658 doi:10.1029/2011JD016599.

659

660 Sezer, T.F., Nuhoglu, A., Bayraktar, H. (2005), Impacts of some meteorological parameters on

661 SO2 and TSP concentrations in Erzurum, Turkey, *Chemosphere*, 59, 1633–1642, doi :

662 http://dx.doi.org/10.1016/j.chemosphere.2005.02.003.

663

664 Sinnhuber, B.-M., Sheode, N., Sinnhuber, M., Chipperfield, M. P., and Feng, W.: The contribution

665 of anthropogenic bromine emissions to past stratospheric ozone trends: a modelling study, *Atmos.*

666   *Chem. Phys.*, 9, 2863-2871, doi:10.5194/acp-9-2863-2009, 2009.

667

668   Smirnov, A., Holben, B. N., Eck, T. F., Dubovik, O., and Slutsker, I.: Cloud-screening and quality

669   control algorithms for the AERONET database, *Remote Sens. Environ.*, 73(3), 337–349, 2000

670

671   Sogacheva, L., Kolmonen, P., Virtanen, T. H., Rodriguez, E., Saponaro, G., and de Leeuw, G.:

672   Post-processing to remove residual clouds from aerosol optical depth retrieved using the

673   Advanced Along Track Scanning Radiometer, Atmos. Meas. Tech., 10, 491-505,

674   doi:10.5194/amt-10-491-2017, 2017.

675

676   Thomas, G.E., Poulsen, C.A., Sayer, A.M., Marsh, S.H., Dean, S.M., Carboni, E., Siddans, R.,

677   Grainger, R.G., Lawrence, B.N. (2009), The GRAPE aerosol retrieval algorithm, *Atmospheric*

678   *Measurement Techniques*, **2**, 679—701, doi: 10.5194/amt-2-679-2009.

679

680   Verstraete, M. M., Pinty, B., & Curran, P. J. (1999). MERIS potential for land applications.

681   *International Journal of Remote Sensing*, 20(9), 1747-1756.

682

683   von Hoyningen-Huene, W., Freitag, M., & Burrows, J. P. (2003). Retrieval of aerosol optical

684   thickness over land surface from top-of-atmosphere radiance. *Journal of Geophysical Research:*

685   *Atmospheres*, 108, D9, doi:10.1029/2001JD002018.

686

687   von Hoyningen-Huene, W., Yoon, J., Vountas, M., Istomina, L. G., Rohen, G., Dinter, T.,

688   Kokhanovsky, A. A., & Burrows, J. P. (2011). Retrieval of spectral aerosol optical thickness over

689   land using ocean color sensors MERIS and SeaWiFS. *Atmospheric Measurement Techniques* , 4,

690   151-171.

691

692   Wilkomirski, B., Sudnik-Wojcikowska, B., Galera, H., Wierzbicka, M. And Malawska, M. (2011),

693   Railway transportation as a serious source of organic and inorganic pollutionn, *Water Air Soil*

694   *Poll.*, 218 (1-4), 333-345, doi : 10.1007/s11270-010-0645-0

695

696   Winkler, P. (1988), The growth of atmospheric aerosol particles with relative humidity, *Phys.*

697   *Scripta*, 37, 223-230, doi:10.1088/0031-8949/37/2/008.

698

699   Zhao, P.S., Zhang, X. L., Xu, X.F. and Zhao, X.J. (2011), Long-term visibility trends and

700   characteristics in the region of Beijing, Tianjin, and Hebei, China, *Atmos. Res.*, 101, 711-718, doi :

701   http://dx.doi.org/10.1016/j.atmosres.2011.04.019.

702

703   Zheng, G. J., Duan, F. K., Su, H., Ma, Y. L., Cheng, Y., Zheng, B., Zhang, Q., Huang, T., Kimoto,

704   T., Chang, D., Pöschl, U., Cheng, Y. F., and He, K. B. (2015), Exploring the severe winter haze in

705   Beijing: the impact of synoptic weather, regional transport and heterogeneous reactions, *Atmos.*

706   *Chem. Phys.*, 15, 2969-2983, doi:10.5194/acp-15-2969-2015.